Volume 8
Number 25
7 July 2020
Pages 5371–5554

Journal of Materials Chemistry B

Materials for biology and medicine

rsc.li/materials-b

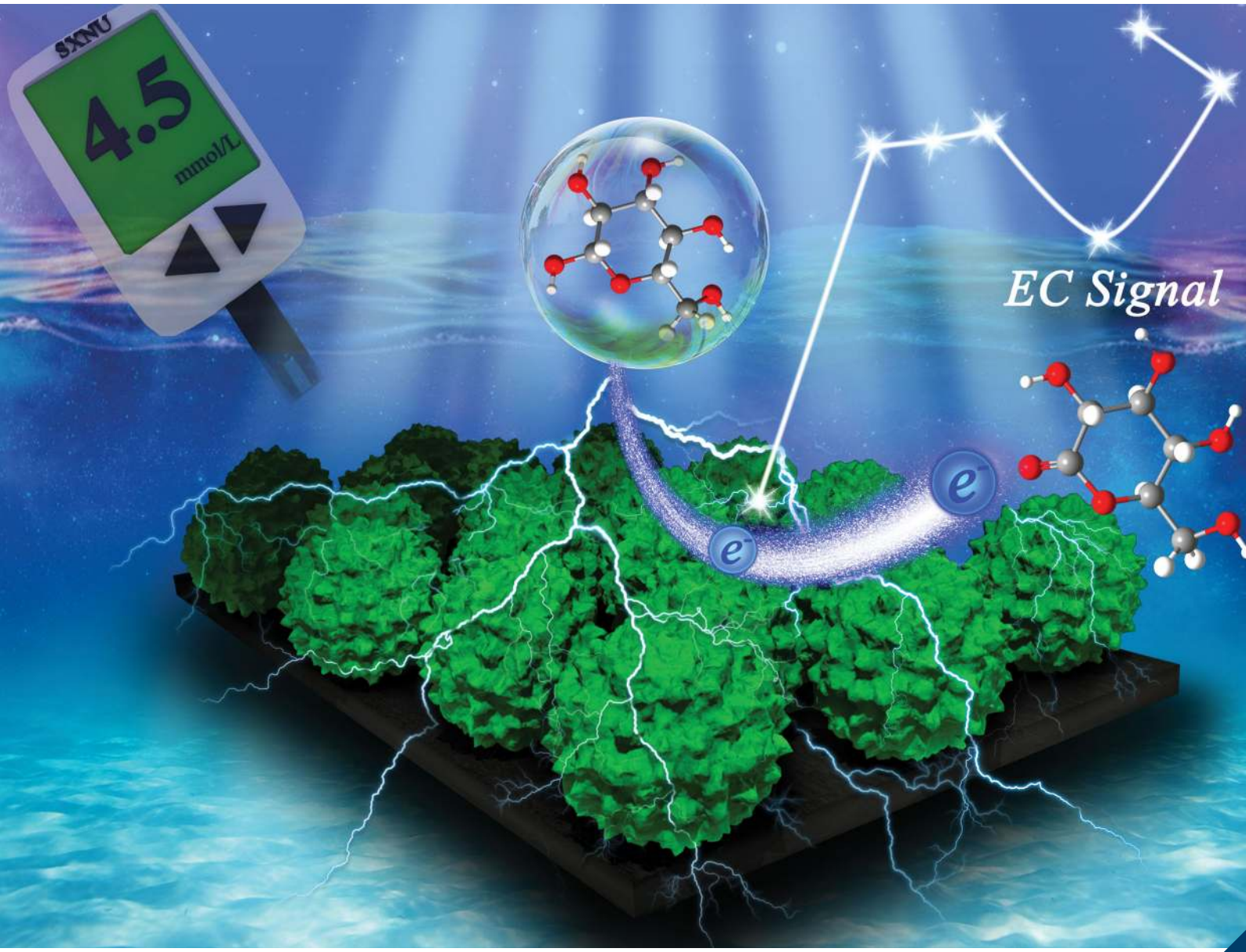

ISSN 2050-750X

ROYAL SOCIETY OF CHEMISTRY

COMMUNICATION

Wenbo Lu, Xuping Sun *et al.*

High-performance non-enzymatic glucose detection: using a conductive Ni-MOF as an electrocatalyst

Journal of Materials Chemistry B

ROYAL SOCIETY OF CHEMISTRY

COMMUNICATION

View Article Online
View Journal | View Issue

Cite this: J. Mater. Chem. B, 2020, 8, 5411

Received 14th January 2020,
Accepted 7th May 2020

DOI: 10.1039/d0tb00131g

rsc.li/materials-b

High-performance non-enzymatic glucose detection: using a conductive Ni-MOF as an electrocatalyst†

Yanxia Qiao,[a] Qian Liu,[b] Siyu Lu,[c] Guang Chen,[d] Shuyan Gao,[e] Wenbo Lu *[a] and Xuping Sun *[b]

Conductive metal–organic frameworks (MOFs) have been studied extensively in applications like water electrolysis, gas storage, and supercapacitors due to their high conductivity and large pore volume. In this communication, we report the first use of a conductive Ni-MOF as a non-noble-metal catalyst for efficient electro-oxidation of glucose in alkaline electrolyte. As an electrochemical sensor for glucose detection, this Ni-MOF shows a fast response time of less than 3 s, a low detection limit of 0.66 μM (S/N = 3), and a high sensitivity of 21 744 μA mM^{-1} cm^{-2}. This glucose sensor also displays excellent selectivity, stability and reproducibility, and its application for the detection of glucose in real samples is also demonstrated successfully.

Glucose (Glu) is an important component of human physiological liquid, and its content is related to the normal metabolism of the human body. High levels of glucose can lead to diabetes, posing a serious threat to human health.[1] For this reason, efficient methods are highly required for the accurate and reliable detection of glucose concentration,[2] which has stimulated the development of colorimetric,[3,4] optical,[5] acoustic,[6] fluorescent,[7] surface plasmon resonance[8] and electrochemical sensing.[9–13] Among these methods, electrochemical sensing has attracted more and more attention because of its plentiful advantages such as a fast response, simple equipment and portability.[14–16] Enzyme-based electrochemical sensors have excellent sensitivity and selectivity, however their wide applications are limited by the high cost, poor immobilization and inherent instability of natural enzymes.[17]

To avoid such issues, much effort has been put into developing earth-abundant inorganic and organic nanocatalysts for direct Glu electro-oxidation for non-enzymatic sensing. Metal–organic frameworks (MOFs), composed of metal ions and organic ligands,[18] have received tremendous attention due to their ordered and adjustable porous structures, large surface areas and numerous active sites.[19–26] However, such compounds usually suffer from poor conductivity and stability, which hinders their electrochemical applications.[27,28]

Conductive MOFs consisting of benzene- or triphenylene-derived ligands possess adjacent disubstituted N, O, or S donor atoms and diverse transition metals, which form π-conjugated materials.[29] Due to the highly conjugated and delocalized π-bond in the ligand, this structure can guarantee electron transport and thus greatly enhance conductivity.[30] However, until now, the use of a conductive MOF for non-enzymatic glucose detection has barely been reported. Here, we demonstrate that a conductive Ni-MOF, a kind of 3D π-conjugated MOF composed of nickel salt and HHTP (2,3,6,7,10,11-hexahydroxytriphenylene), can efficiently catalyze glucose oxidation in alkaline media. Under optimized conditions, the conductive Ni-MOF exhibits a wide detection range from 0.001 to 8 mM, a low detection limit (0.66 μM, S/N = 3), high sensitivity (21 744 μA mM^{-1} cm^{-2}) and a fast response time (3 s). Meanwhile, this sensor shows excellent selectivity, stability and reproducibility. It can also be used to monitor glucose in real samples.

The 3D conductive Ni-MOF was prepared by a facile method (the details are shown in the ESI†). As shown in Fig. 1a, the honeycomb lattices are made from HHTP ligands with ortho-disubstituted O donor atoms that define square-planar coordination environments with the Ni^{2+} nodes.[28] The inset of Fig. 1a shows the structure of HHTP. Fig. 1b shows the X-ray diffraction (XRD) pattern of the synthesized $Ni_3(HHTP)_2$. The existence of sharp peaks located at small angles of $2\theta = 4.5^\circ$, 9.5°, 12.6° and 17° can be indexed to the

[a] Key Laboratory of Magnetic Molecules and Magnetic Information Materials (Ministry of Education), School of Chemistry and Material Science, Shanxi Normal University, Linfen 041004, China. E-mail: luwb@sxnu.edu.cn
[b] Institute of Fundamental and Frontier Sciences, University of Electronic Science and Technology of China, Chengdu 610054, Sichuan, China. E-mail: xpsun@uestc.edu.cn
[c] Green Catalysis Center and College of Chemistry, Zhengzhou University, Zhengzhou 450001, Henan, China
[d] The Key Laboratory of Life-Organic Analysis and Key Laboratory of Pharmaceutical Intermediates and Analysis of Natural Medicine, School of Chemistry and Chemical Engineering, Qufu Normal University, Qufu 273165, Shandong, China
[e] School of Materials Science and Engineering, Henan Normal University, Xinxiang 453007, Henan, China

† Electronic supplementary information (ESI) available: Experimental section and supplementary figures. See DOI: 10.1039/d0tb00131g

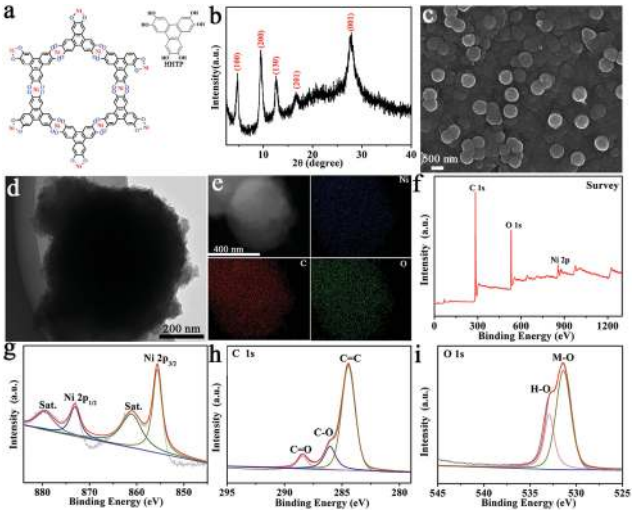

Fig. 1 (a) Connecting mode of HHTP molecules and Ni^{2+} ions (inset: the structural formula of HHTP). (b) XRD pattern of the conductive Ni-MOF. (c) SEM image of the conductive Ni-MOF. (d) TEM image of one single conductive Ni-MOF nanosphere. (e) EDX elemental mapping images of Ni, C, and O of the conductive Ni-MOF. (f) XPS survey spectrum of the conductive Ni-MOF. XPS spectra of the conductive Ni-MOF in the (g) Ni 2p, (h) C 1s and (i) O 1s regions.

(100), (200), (130) and (201) planes, respectively,[31,32] revealing the long-range order within the square-planar plane. The apparent peak at $2\theta = 27.3^{\circ}$ can be indexed to the (002) plane, demonstrating the long-range order along the axis, as anticipated for covalently linked layered materials, and it indicates π–π layered stacking.[33–35] We provide the XRD pattern of the conductive Ni-MOF after long-term tests in Fig. S2 (ESI†). As expected, the peaks show no obvious change, suggesting excellent structure stability. The scanning electron microscopy (SEM) image indicates that the conductive Ni-MOF nanosphere has an average diameter size of about 400 nm (Fig. 1c). In addition, the pore structure and specific surface area results of the Ni-MOF were obtained by using the Brunauer–Emmett–Teller (BET) method, as shown in Fig. S4 (ESI†). BET surface area is 12.1467 $m^2 g^{-1}$ based on the nitrogen adsorption/desorption isotherms. The pore size is mainly distributed in the range of 2–9 nm. As shown in Fig. 1d, the transmission electron microscopy (TEM) image further confirms the morphology and size. The scanning TEM (STEM) image and energy-dispersive X-ray (EDX) elemental mapping images confirm the uniform distribution of Ni, C, and O elements (Fig. 1e). To obtain detailed elemental compositions of the conductive Ni-MOFs, X-ray photoelectron spectroscopy (XPS) analysis was further performed. Fig. 1f shows the characteristic spin–orbit peaks of Ni 2p, C 1s and O 1s. As shown in Fig. 1g, the binding peaks at around 855.70 eV and 862.10 eV are attributed to Ni $2p_{3/2}$ and its satellite peaks. The binding peaks at approximately 873.80 eV and 879.80 eV are assigned to Ni $2p_{1/2}$ and its satellite peaks, respectively.[30] These results indicate that nickel ions exist in a divalent state (Ni^{2+}). Fig. 1h shows the C 1s spectrum; the peak at 284.45 eV is considered to represent the C=C bond of phenyl carbons. The peaks at 286.05 eV and 288.43 eV are ascribed to the C–O bond and the C=O bond, resepectively.[35] These two distinct types of O are expected for a charge neutral molecule in which the HHTP ligand can adapt semiquinone and quinone structures.[36] Fig. 1i shows the O 1s spectrum; the peak at around 531.40 eV can be attributed to the characteristic metal–oxygen bond (M–O). The other peak at 532.94 eV corresponds to oxygen in surface hydroxyl groups (H–O).[37] All these XPS results confirm the formation of the conductive Ni-MOF.

All electrochemical measurements were performed using an electrochemical workstation (CHI 660E) in a conventional three electrode system at room temperature. The conductive Ni-MOF was used as a working electrode, and platinum wire and saturated Ag/AgCl served as the counter electrode and reference electrode, respectively. All the potentials reported in this work are reported relative to the Ag/AgCl electrode. The electrochemical responses at different pH of the conductive Ni-MOF towards 1 mM glucose were studied (Fig. S5, ESI†). It can be seen from the plot that the anodic peak current increases with the change of pH from 10 to 14. When the pH value is 14, the strong alkaline environment is non-friendly to the sensor. Thus, pH 13 was used for the optimal electrolyte solution in the following tests. Fig. 2a shows the cyclic voltammograms (CVs) of the conductive Ni-MOF in 0.1 M NaOH in the absence and presence of 1 mM glucose, and blank cloth paper (CP) and Nafion supplemented with 1 mM glucose at a scan rate of 20 mV s^{-1} in the potential range from 0 to 0.8 V. As observed, bare CP and Nafion give no enhancement in redox current with the addition of 1 mM glucose. In contrast, the conductive Ni-MOF exhibits an obvious oxidation peak in the presence of 1 mM glucose; the enhancement of the anodic current is due to the electro-oxidation

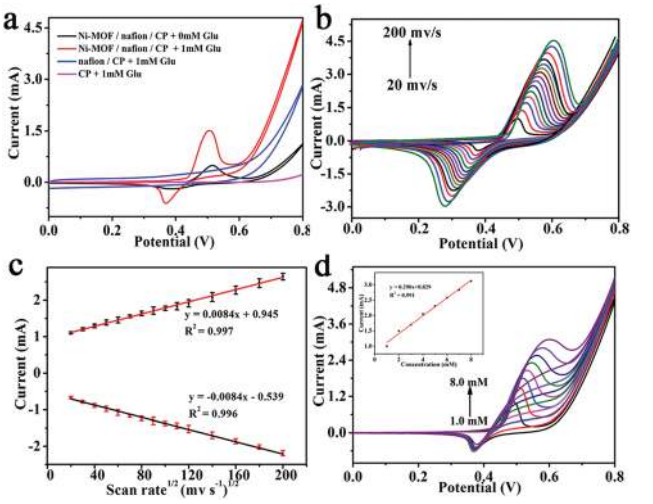

Fig. 2 (a) CV curves of the conductive Ni-MOF in the absence and presence of 1 mM glucose, and blank cloth paper (CP) and Nafion supplemented with 1 M glucose in 0.1 M NaOH (scan rate: 20 mV s^{-1}). (b) CV curves of the conductive Ni-MOF supplemented with 1 mM glucose at scan rates from 20 to 200 mV s^{-1}. (c) Corresponding calibration curves of the anodic and cathodic peak currents and square root of scan rates. (d) CV curves obtained after the addition of different concentrations of glucose from 1 to 8 mM in 0.1 M NaOH (scan rate: 20 mV s^{-1}), inset: the corresponding calibration curve.

of glucose with the participation of Ni^{3+}. The mechanism can be explained as follows:

$$\text{Ni(II)-MOF} \rightarrow \text{Ni(III)-MOF} + e^-$$

$$\text{Ni(III)-MOF} + OH^- + \text{glucose} \rightarrow \text{Ni(II)-MOF} + \text{gluconolactone} + H_2O + e^-$$

Fig. 2b shows that the anodic and cathodic peak currents increase with different scan rates in the range of 20–200 mV s^{-1}. The results indicate that the anodic peaks shift to a more positive value, while cathodic peaks shift to a more negative value. Meanwhile, Fig. 2c shows the good linear relationship between peak currents and the square root of scan rate. This implies a diffusion-controlled process of glucose oxidation on the conductive Ni-MOF electrode, which is an ideal case in quantitative analysis. Fig. 2d shows CVs of the conductive Ni-MOF in solutions with different glucose concentrations in the potential range of 0 to 0.8 V. The corresponding calibration curve of the anodic peak current is linearly dependent (R^2 = 0.991) on the concentration of glucose ranging from 1.0 to 8.0 mM (the inset of Fig. 2b). This confirms the excellent electrocatalytic performance for glucose detection.

Fig. 3a shows the amperometric response of the conductive Ni-MOF with the successive addition of glucose at different potentials (from 0.45 to 0.60 V). With the increase of the applied potential, the current response increases significantly, but the noise signal is more pronounced at 0.6 V. So, we chose 0.55 V as the best applied potential. Fig. 3b shows the amperometric response to the consecutive injection of glucose in different concentrations in 0.1 M NaOH at 0.55 V. The inset of Fig. 3b shows the amperometric response to low glucose concentrations from 1 to 30 μM. Fig. 3c shows that this sensor possesses a fast amperometric response towards glucose detection and it can achieve steady state current within 3 s. Fig. 3d shows the corresponding standard curve of current with various concentrations obtained from the current–time curve. The inset of Fig. 3d shows the corresponding standard curve between the current and low concentration glucose (0.001–0.5 mM) at an applied voltage of 0.55 V. Moreover, the detection limit (LOD) was calculated to be 0.66 μM; LOD can be calculated using LOD = $3\sigma/S$, where σ is the standard deviation of the response, and S is the slope of the calibration curve. The sensitivity was calculated as 21 744 μA mM^{-1} cm^{-2}. Compared to other electrode materials (Table S1, ESI†), the conductive Ni-MOF displays a lower detection limit and higher sensitivity. These results suggest that the conductive Ni-MOF is a promising material for developing non-enzymatic glucose sensors.

To demonstrate its feasibility for the analysis of practical samples, we applied the conductive Ni-MOF electrode to detect glucose in human blood serum (Fig. 4a) and peach juice (Fig. S6, ESI†). Fig. 4a shows that the oxidation peak currents increase with the successive addition of glucose in the range of 1 to 8 mM into a diluted human blood serum sample. The corresponding calibration curve (Fig. 4b) indicates that the peak current increases with increasing glucose concentration in the range from 1 to 8 mM. Meanwhile, results measured by the hospital and by using the conductive Ni-MOF are listed in Table S2 (ESI†) for comparison. The relative standard deviation (RSD) and bias are less than 4% and 0.20 mM, respectively. The results demonstrate that this glucose sensor based on a conductive Ni-MOF is promising for practical sample testing. Anti-interference property is an important parameter for glucose sensors.[38,39] Since human blood contains many compounds like urea, lactose (Lac), uric acid (UA) and others,

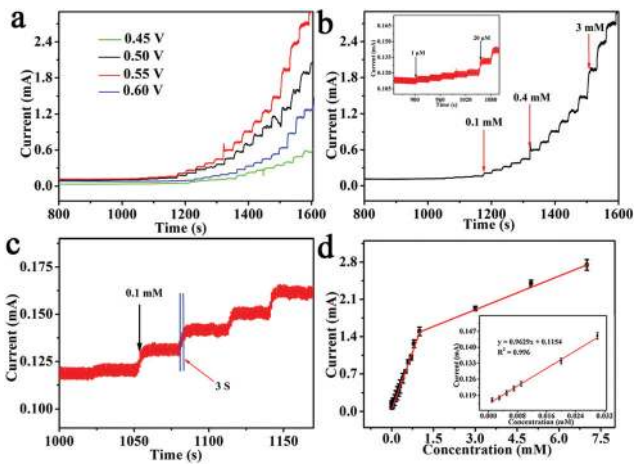

Fig. 3 (a) Amperometric response of the conductive Ni-MOF upon the successive addition of glucose at different applied potentials. (b) Amperometric response of the conductive Ni-MOF upon successive injection of glucose with different concentrations in 0.1 M NaOH solution at 0.55 V (inset: amperometric response of the conductive Ni-MOF at low glucose concentrations). (c) The response time curve of glucose at different concentrations. (d) Corresponding standard curves of current with various concentrations obtained from the i–t curve (inset: the corresponding calibration curve of the conductive Ni-MOF at low glucose concentrations).

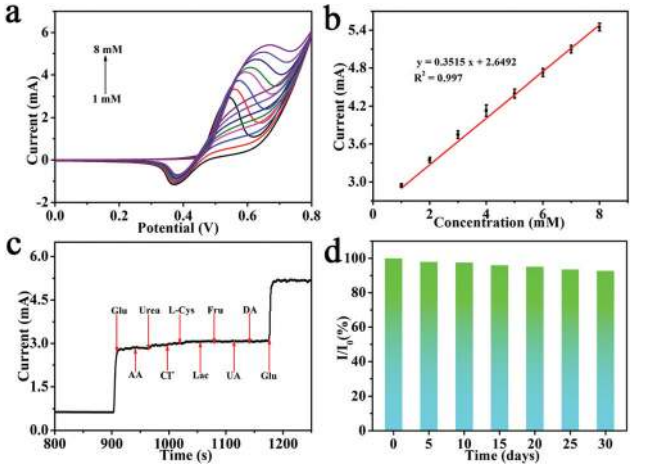

Fig. 4 (a) CV curves obtained after the addition of different concentrations of glucose from 1 to 8 mM in 0.1 M NaOH containing 20% human blood serum (scan rate: 20 mV s^{-1}). (b) Calibration curve of the oxidation peak current response to different glucose concentrations. (c) Amperometric response of the conductive Ni-MOF upon the addition of 1 mM glucose and various interference species (2 mM AA, 2 mM urea, 2 mM Cl^-, 2 mM L-Cys, 2 mM Fru, 2 mM UA and 2 mM DA) in 0.1 M NaOH at 0.55 V. (d) Long-period stability of the glucose sensor over a number of days (5–30 days).

which are easily oxidized, their effects cannot be ignored. Fig. 4c presents the amperometric response of the conductive Ni-MOF electrode at 0.55 V with the successive addition of 1 mM glucose, 2 mM ascorbic acid (AA), 2 mM urea, 2 mM Cl^-, 2 mM L-cysteine (L-Cys), 2 mM Lac, 2 mM fructose (Fru), 2 mM UA, 2 mM dopamine (DA), and 1 mM glucose in 0.1 M NaOH. A distinct glucose response can be observed while insignificant responses to the interfering species are obtained, indicating that the electrode has high selectivity. Fig. 4d shows the long-term stability of the conductive Ni-MOF in 0.1 M NaOH. The conductive Ni-MOF was stored in air and the current response was tested every five days. This sensor maintains 92.8% of its original current after 30 days. Meanwhile, the reproducibility of the conductive Ni-MOF was also investigated by measuring the current response to 1 mM glucose using five conductive Ni-MOF electrodes. The relative standard deviation of anodic peak current is only 3.75%, demonstrating a good reproducibility, as shown in Fig. S7 (ESI†). In summary, the conductive Ni-MOF is proven as an efficient catalyst for the electro-oxidation of glucose. As an electrochemical sensor for non-enzymatic glucose detection, this Ni-MOF shows a fast response time within 3 s, a low detection limit of 0.66 μM (S/N = 3), and a high sensitivity of 21 744 μA mM^{-1} cm^{-2}, with excellent selectivity, stability and reproducibility. Our study not only provides an attractive low-cost catalyst for high-performance glucose determination, but also opens up an exciting new avenue for designing and developing conductive MOFs as superb sensors for the electrochemical detection of small molecules.

Conflicts of interest

There are no conflicts to declare.

Acknowledgements

This work was supported by the National Natural Science Foundation of China (No. 21575137 and 21705103), the Applied Basic Research Project of Shanxi Province (No. 201801D221392), the Graduate Education Innovation Project of Shanxi Province (2018SY057), Collaborative Innovation Center for Shanxi Advanced Permanent Materials (2019-05) and Technology and the 1331 Engineering of Shanxi Province.

References

1 J. Wang, *Chem. Rev.*, 2008, **108**, 814–825.
2 E. V. Karpova, E. V. Shcherbacheva, A. A. Galushin, D. V. Vokhmyanina, E. E. Karyakina and A. A. Karyakin, *Anal. Chem.*, 2019, **91**, 3778–3783.
3 S. Liu, J. Tian, L. Wang, Y. Luo and X. Sun, *RSC Adv.*, 2012, **2**, 411–413.
4 M. N. Karim, S. R. Anderson, S. Singh, R. Ramanathan and V. Bansal, *Biosens. Bioelectron.*, 2018, **110**, 8–15.
5 M. Steiner, A. Duerkop and O. S. Wolfbeis, *Chem. Soc. Rev.*, 2011, **40**, 4805–4839.
6 J. Luo, P. Luo, M. Xie, K. Du, B. Zhao, F. Pan, P. Fan, F. Zeng, Z. Zhang and G. Liang, *Biosens. Bioelectron.*, 2013, **49**, 512–518.
7 J. Tian, S. Liu, Y. Luo and X. Sun, *Catal. Sci. Technol.*, 2012, **2**, 432–436.
8 L. Wang, W. Zhu, W. Lu, X. Qin and X. Xu, *Biosens. Bioelectron.*, 2018, **111**, 41–46.
9 T. Chen, D. Liu, W. Lu, K. Wang, G. Du, A. M. Asiri and X. Sun, *Anal. Chem.*, 2016, **88**, 7885–7889.
10 D. Zhou, X. Cao, Z. Wang, S. Hao, X. Hou, F. Qu, G. Du, A. M. Asiri, C. Zheng and X. Sun, *Chem. – Eur. J.*, 2017, **23**, 5214–5218.
11 Z. Wang, X. Cao, D. Liu, S. Hao, R. Kong, G. Du, A. M. Asiri and X. Sun, *Chem. – Eur. J.*, 2017, **23**, 4986–4989.
12 H. Huo, Y. Zhao and C. Xu, *J. Mater. Chem. A*, 2014, **2**, 15111–15117.
13 Y. Liu, X. Cao, R. Kong, G. Du, A. M. Asiri, Q. Lu and X. Sun, *J. Mater. Chem. B*, 2017, **5**, 1901–1904.
14 D. Kim, J. Moon, W. Lee, J. Yoon, C. S. Chol and Y. Shim, *Biosens. Bioelectron.*, 2017, **91**, 276–283.
15 Y. Li, M. Xie, X. Zhang, Q. Liu, D. Lin, C. Xu, F. Xie and X. Sun, *Sens. Actuators, B*, 2019, **278**, 126–132.
16 S. Liu, J. Tian, L. Wang, Y. Luo, W. Lu and X. Sun, *Biosens. Bioelectron.*, 2011, **26**, 4491–4496.
17 D. Zhai, B. Liu, Y. Shi, L. Pan, Y. Wang, W. Li, R. Zhang and G. Yu, *ACS Nano*, 2013, **7**, 3540–3546.
18 X. Xiao, L. Zou, H. Pang and Q. Xu, *Chem. Soc. Rev.*, 2020, **49**, 301–331.
19 S. T. Meek, J. A. Greathouse and M. D. Allendorf, *Adv. Mater.*, 2011, **23**, 249–267.
20 B. Guan, X. Hao, B. Wu and X. Lou, *Adv. Mater.*, 2017, **29**, 1703614.
21 Q. Liu, L. Xie, X. Shi, G. Du, A. M. Asiri, Y. Luo and X. Sun, *Inorg. Chem. Front.*, 2018, **5**, 1570–1574.
22 D. Li, H. Xu, L. Jiao and H. Jiang, *EnergyChem*, 2019, **1**, 100005.
23 H. Zhang, W. Zhao, M. Zou, Y. Wang, Y. Chen, L. Xu and A. Cao, *Adv. Energy Mater.*, 2018, **8**, 1800013.
24 H. Furukawa, N. Ko, Y. B. Go, N. Aratani, S. B. Choi, E. Choi, A. O. Yazaydin, R. Q. Snurr, M. O'Keeffe, J. Kim and O. M. Yaghi, *Science*, 2010, **329**, 424–428.
25 W. Zhou, S. Lv, X. Liu, Y. Li and J. Liu, *Chem. Commun.*, 2019, **55**, 11207–11210.
26 Y. Li, Y. Xu, Y. Liu and H. Pang, *Small*, 2019, **15**, 1902463.
27 Z. Liang, R. Zhao, T. Qiu, R. Zou and Q. Xu, *EnergyChem*, 2019, **1**, 100001.
28 W. Li, J. Lv, Q. Li, J. Xie, N. Ogiwara, Y. Huang, H. Jiang, H. Kitagawa, G. Xu and Y. Wang, *J. Mater. Chem. A*, 2019, **7**, 10431–10438.
29 V. Rubio-Giménez, N. Almora-Barrios, G. Escorcia-Ariza, M. Galbiati, M. Sessolo, S. Tatay and C. Martí-Gastaldo, *Angew. Chem., Int. Ed.*, 2018, **57**, 15086–15090.
30 J. Yang, P. Xiong, C. Zheng, H. Qiu and M. Wei, *J. Mater. Chem. A*, 2014, **2**, 16640–16644.
31 M. Ko, L. Mendecki and K. A. Mirica, *Chem. Commun.*, 2018, **54**, 7873–7891.

32 B. Hoppe, K. D. J. Hindricks, D. P. Warwas, H. A. Schulze, A. Mohmeyer, T. J. Pinkvos, S. Zailskas, M. R. Krey, C. Belke, S. König, M. Fröba, R. J. Haug and P. Behrens, *CrystEngComm*, 2018, **20**, 6458–6471.
33 T. Li, W. Zhang, Y. Liu, Y. Li, C. Cheng, H. Zhu, X. Yan, Z. Li and Z. Gu, *J. Mater. Chem. A*, 2019, **7**, 19676–19681.
34 M. Hmadeh, Z. Lu, Z. Liu, F. Gándara, H. Furukawa, S. Wan, V. Augustyn, R. Chang, L. Liao, F. Zhou, E. Perre, V. Ozolins, K. Suenaga, X. Duan, B. Dunn, Y. Yamamto, O. Terasaki and O. M. Yaghi, *Chem. Mater.*, 2012, **24**, 3511–3513.
35 H. Wu, W. Zhang, S. Kandambeth, O. Shekhah, M. Eddaoudi and H. N. Alshareef, *Adv. Energy Mater.*, 2019, **9**, 1900482.
36 L. Mendecki and K. A. Mirica, *ACS Appl. Mater. Interfaces*, 2018, **10**, 19248–19257.
37 Q. Chen, S. Lei, P. Deng, X. Ou, L. Chen, W. Wang, Y. Xiao and B. Cheng, *J. Mater. Chem. A*, 2017, **5**, 19323–19332.
38 Z. Wang, X. Cao, D. Liu, S. Hao, G. Du, A. M. Asiri and X. Sun, *Chem. Commun.*, 2016, **52**, 14438–14441.
39 F. Xie, X. Cao, F. Qu, A. M. Asiri and X. Sun, *Sens. Actuators, B*, 2018, **255**, 1254–1261.